

CLIMATOLOGY

A 1600-year record of extreme rainfall in northern Arabia

Sam J. Purkis^{1*}, Steven N. Ward², Bolton J. Howes¹, Jake M. Longenecker¹, Morgan I. Chakraborty¹, Akos Kalman¹, Amy C. Clement¹, Arash Sharifi^{1,3}, Francesca Benzoni⁴, Christopher Clarke⁴, Mattie Rodrigue⁵

Intense rain can trigger flashfloods in Arabia. Torrential rains in 2024 sowed widespread chaos in the region. Sediment-loaded plumes discharged by flashfloods deposit onto the seabed. Burrowing animals disrupt these flood layers, erasing the paleorainfall record. Fortunately, we discovered an anoxic deep-sea brine pool sited close enough to shore to chronicle floods, yet be otherwise undisturbed by animals. Cores retrieved from the pool delivered a 1600-year rainfall record. We merge these core-layer histories with modern rainfall statistics, satellite observations, and simulations to deliver a high-resolution quantitative Late Holocene hydroclimate record for Arabia. We find that the modern era is 2.5 times drier than the last 1.6 thousand years. The Little Ice Age stands out as particularly wet. That period experienced a fivefold increase in rainfall intensity compared to today. Though hyperarid now, the flood layers demonstrate that climate shifts can generate weather conditions unwitnessed in the modern era. Such long-range insight is crucial for framing uncertainties surrounding future hydroclimate forecasts.

INTRODUCTION

Even basic data on modern rainfall in Arabia are sparse. Scarcer still are paleo-rainfall reconstructions. Catastrophic flooding across the Arabian Peninsula in the winter of 2024 adds urgency to understanding the frequency and triggers of such severe weather. Speleothems, tree rings, and geochemical analyses provide useful proxies, but only deliver qualitative notions of “wetter” or “drier” climate (1–3). To close this gap, we provide a quantitative high-fidelity record of Late Holocene Arabian rainfall.

Arabia is noteworthy for its high climate variability during the Holocene, an era considered to be relatively stable (4, 5). Accordingly, scientists cast the Middle East as a climate change hot spot (6, 7) and a key calibration point for climate models (8–10). We focus on the Gulf of Aqaba, an extension of the northern Red Sea. This region is usually hyperarid, but rare and intense winter rains can drop several years of precipitation in only a few hours (11). Such storms fill high mountain watersheds, activate ephemeral rivers called “wadis,” and transport freshwater plumes laden with terrigenous sediments into the sea (12, 13) (Fig. 1). These plume clouds spread out, then settle to the seabed as classic fining-upward (Bouma-type) sequences. The fining-upward nature of individual beds conveniently distinguishes each event from preceding ones. Thus, counting and dating the terrigenous layers in seabed cores offers a means of reconstructing regional rainfall over geological timescales.

The extraction of environmental signals from sedimentary layers is complicated by the buffering and shredding of these signals during sediment transport and the often incomplete nature of the stratigraphic record (14). Moreover, the reworking of marine sediments by burrowing animals (bioturbation) confounds linking flood

deposits in cores to hydroclimate. Steiner *et al.* (15) emphasizes how bioturbation effectively erases short-term events from the deep Gulf’s sedimentary record. Their study, as well as Katz *et al.* (16) and Bialik *et al.* (17), advise that biological activity can mix decades of sediment deposition. Bioturbation also limited the fidelity of the Red Sea rainfall record retrieved by Arz *et al.* (1). Those authors only report broad precipitation trends played out over millennia.

The deep-sea “NEOM” brine pool discovered by Purkis *et al.* (18) at a water depth of 1770 m in the Gulf of Aqaba (Fig. 2 and Supplementary Materials) offers a unique opportunity to quantify the region’s hydroclimate at exceptionally high resolution. The pool is located just 2 km from the coast, perfectly positioned to receive terrigenous outwash. Given the absence of a meaningful terrigenous transfer zone or continental shelf, the NEOM brine pool is particularly sensitive to flood events, allowing for rapid, high-fidelity transmission of environmental signals from terrestrial to marine settings. In addition, the anoxia, low pH, and hypersalinity of the brine excludes all animals. Thus, sedimentary sequences accumulated on the bed of the NEOM pool are entirely unaffected by bioturbation. The short source-to-sink distance and exquisitely preserved sedimentary layering combine to allow a successful extraction of environmental signals from sedimentary rocks. In this study, we reconstruct rainfall histories from two brine pool cores to deliver a high-resolution quantitative Late Holocene hydroclimate record for northern Arabia. These data provide an important benchmark for the interpretation of qualitative rainfall proxies from the larger region.

RESULTS

Contemporary hydroclimate of the brine pool watershed

While our goal is to extract historical rainfall rates from the core layers, let us first consider modern rainfall rates. The closest research-grade rain gauge to the NEOM pool is located 90 km to the north in Eilat (Israel). To quantify precipitation at our site, we instead use the NASA multisatellite GPM-IMERG v.6 dataset that has a 30-min time interval and a 10 by 10 km spatial resolution (19). “Final Run” versions

¹Rosenstiel School of Marine, Atmospheric, and Earth Science, University of Miami, Miami, FL 33149, USA. ²Institute of Geophysics and Planetary Physics, University of California Santa Cruz, Santa Cruz, CA 95064, USA. ³Beta Analytic Inc., Isobar Science, Miami, FL 33155, USA. ⁴King Abdullah University of Science and Technology, Thuwal, Saudi Arabia. ⁵OceanX, New York, NY 10018, USA.

*Corresponding author. Email: spurkis@earth.miami.edu



Fig. 1. Sediment plumes following a flashflood. Situated 10 km south of the brine pool, Wadi Al Tayyib (A) experienced a violent flashflood during the 25 October 2018 41-mm rain event. PlanetScope satellite imagery acquired before (B) and after the event (C) shows a sediment plume drifting offshore for at least 1 day after the storm. (D) The source of this plume on the day of the flood, with a torrent of sediment-laden water emanating from the wadi, crossing the coastal road, and pouring into the Gulf of Aqaba. (E and F) Photographs taken during the flood looking west, down the wadi, and east, up it.

of these data integrate precipitation estimates from multiple satellites and are calibrated globally from rain gauges. Final Run data span June 2000 to September 2021.

Nine IMERG pixels cover the 22 catchments in the 300-km² wadi watershed. Each pixel provides a separate measure of rainfall over the 7791-day record. Cumulative probability of annual rainfall indicate that the nine records behave in a similar fashion (Fig. 3). Average annual rainfall across the nine pixels ranges from 29.70 mm/year (pixel #8) to 33.60 mm/year (pixel #4). Average annual rainfall rate across all pixels is 31.33 mm/year. Differential probability of annual rainfall for each of the nine pixels shows distinctly non-Gaussian long-tailed distributions with high coefficients of variation [between 0.66 (pixel #1) and 0.86 (pixel #8)]. Fully 30% of the years have annual rainfall less than half the 31-mm mean, while more than 15% of the years have rainfalls exceeding twice the mean. Large year-to-year variation, both high and low, compared to average values typifies arid landscapes where few, but fierce, rain events dominate.

IMERG captured 1580 rain events in the watershed. The blue dots (Fig. 4A) map their recurrence statistics. Giving some consistency, the 68-year Eilat rain gauge dataset (red line) aligns closely with the IMERG record. Counts of events depositing >5 mm of rain

in a 365-day moving window (Fig. 4B) shows the winters of 2000 to 2010 to be relatively dry compared to the wet winters of 2010 to 2021. The most severe event in the IMERG record occurred on 25 October 2018, dropping 41.23 mm of rain averaged across the pool's watershed (Fig. 4C).

Late Holocene rainfall frequency and intensity

Our brine pool cores contain 137 flood layers dating from 504 to 1817 CE (Common era) (Fig. 5A, Supplementary Materials, and figs. S1 and S2). Unfortunately, layers deposited after 1821 are disturbed, perhaps by the action of retrieving the core, or by the shaking of the 7.2 M_w (moment magnitude) 1995 Nuweiba earthquake that struck just 10 km away (20, 21).

Figure 5B plots a running 100-year average of the number of flood layers and thickness production versus time. The figure also identifies three major climate events: the "Dark Ages Cool Period" (500 to 900 CE), "Medieval Warm Period" (900 to 1300 CE), and the "Little Ice Age" (1400 to 1850 CE). The frequency and thickness production of flood layers (6 and 10 mm per century, respectively) during the Dark Ages Cool Period are the lowest of the three periods. During the early part of the Medieval Warm Period, the number and

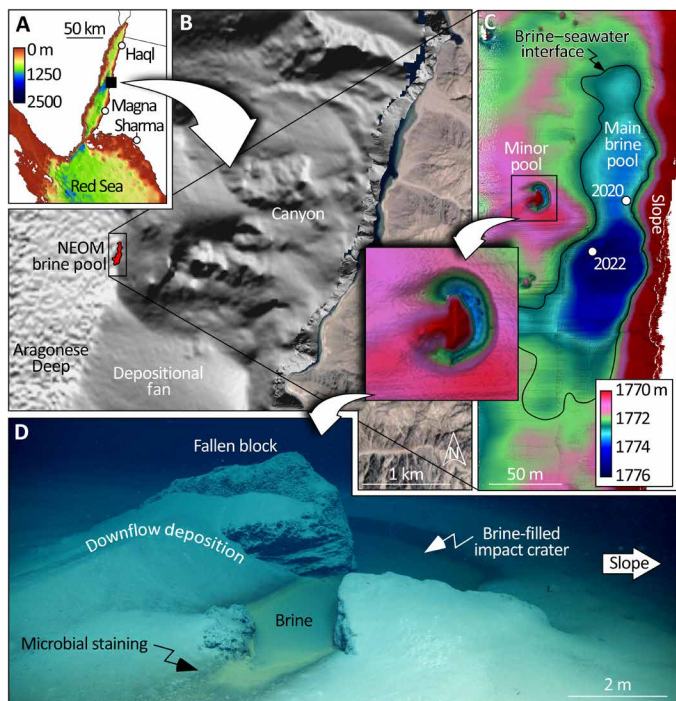


Fig. 2. Depositional setting of the NEOM brine pool. (A) The brine pool is located in 1772 m water at the toe-of-slope of the Saudi coastal margin in the Aragonese Deep. The pool, situated just 2 km from the coast, is excellently positioned to receive fluvial outwash (B). Multibeam acquired from a remotely operated vehicle (C) shows the pool to be 10,000 m² in area and 6 m deep. Centimeters of sediment softly blanketing the area paint a stable recent environment. Whether the sedimentation was continuous or episodic farther back in history, only coring can reveal. We acquired two cores through the bed of the pool (white circles). Smaller pools have been created by blocks falling down slope (D), which subsequently fill with brine.

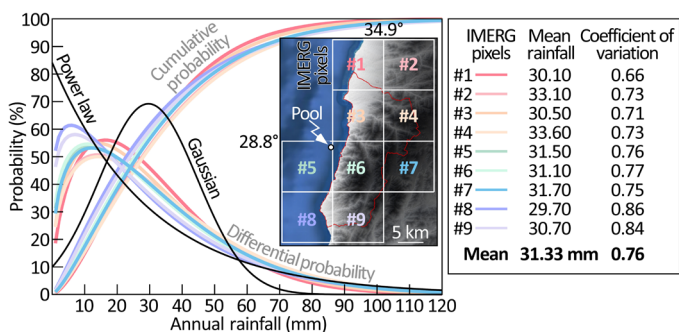


Fig. 3. Weibull fits to annual rainfall recorded in each of the nine IMERG pixels covering the NEOM watershed over the 21-year climatology of this dataset. All records show mean values of about 30 mm/year with a high coefficient of variation delivering non-Gaussian long-tailed distributions. The black lines plot Gaussian and power law ($P \geq 10^{-bn}$) differential probability with means of 30 mm/year. You can see that both the power law and the Weibull fits have higher likelihoods of extremely wet and dry years versus the mean than would be expected from the Gaussian. Compared to the consistent precipitation experienced by wetter regions, arid landscapes tend to be dominated by more frequent drought and flood years.

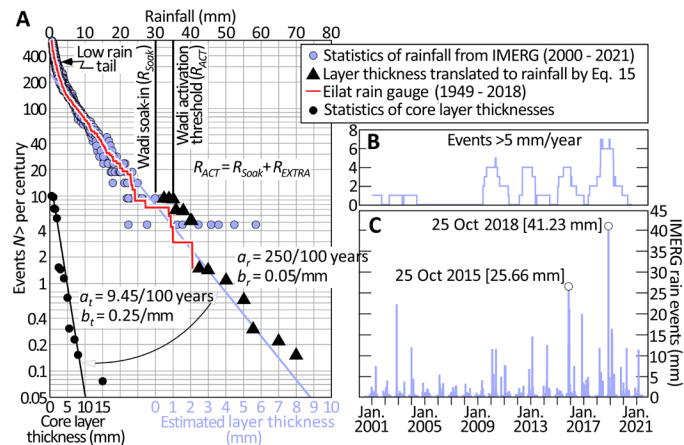


Fig. 4. Rainfall and core statistics for the brine pool. (A) Plots thickness statistics of the core's flood layers (black dots), which are well fit by a power law distribution with slope $b_t = 0.25/\text{mm}$. Rainfall statistics (2000 to 2021) from the nine IMERG pixels covering the brine pool's 300-km² watershed (blue dots) are also well fit by a power law, this time with a slope, b_r , of 0.05/mm. Rain gauge data from Eilat (red line) align with the IMERG satellite prediction. Core layer thicknesses (black triangles) translated to rainfall rates by Eq. 21 (Materials and Methods). Note the steepening of the IMERG and Eilat records for rains <3 mm. This is the low rain tail. (B) Number of rain events >5 mm per year. (C) The intensity of the IMERG rain events. The most severe storm occurred on 25 October 2018 dropping 41.23 mm of rain into the pool's catchment.

thickness production of flood layers increased to 12 and 25 mm per century. The Little Ice Age contained the highest concentration of layers and production (17 floods and 35 mm per century). The peak layer concentration (24 per century) centers around 1500 CE.

A simple notion envisions periods with a higher layer concentration or thickness production generally correspond to wetter epochs. To date, though, no one has been able to extend this notion beyond a relative sense. We propose four methods to quantify this concept (see Materials and Methods). Figure 5C shows the average annual rainfall in millimeters per year over a sliding 100-year window for those four methods. They all speak to a marked increase in annual rainfall initiating at 1400 CE. Peak rates are reached by 1500 CE with an annual rainfall of more than 150 mm/year, five times greater than the modern value of 31 mm/year. Rates then decline to three times the modern value (~90 mm/year) by the end of the core record (1850 CE). The entire core saw rainfalls 2.5 times greater than today. Clearly, the modern era is drier than any time in the Late Holocene.

How do the rainfall estimates from the brine pool fit into the broader picture of Holocene climate? Total solar irradiance (TSI) is a commonly accepted driver of Late Holocene climate. Lean's (22) estimate of TSI (orange curve, Fig. 5C) was derived from analyzing cosmogenic isotopes extracted from ice cores and tree rings. From a high around 950 CE, TSI oscillates around a downward trend to modern times. Four pronounced solar irradiance drops [labeled (i) through (iv)] are evident. The first pair occur at the beginning and end of the Medieval Warm Period. The third low marks the onset of the Little Ice Age and the final low occurs midway through it.

Is there any connection between our NEOM rainfall histories and TSI? The Lean (22) irradiance record and our rainfall reconstructions overlap from 850 to 1810 CE. For this time span, both spectral and correlation methods can assess coherence. In this exercise, bear in mind that the rainfall and TSI histories originate from

Downloaded from https://www.science.org at University of Washington on March 10, 2025

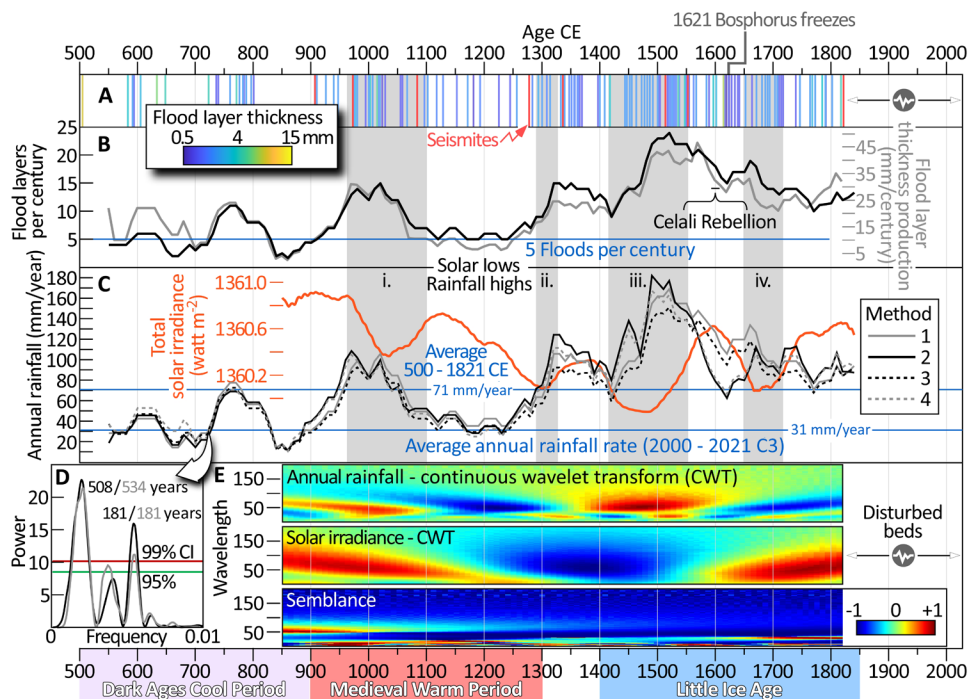


Fig. 5. Late Holocene rainfall frequency, intensity, and solar forcing. (A) Temporal distribution of core flood layers color coded by layer thickness. (B) Number of floods and layer thickness production tallied in 100-year moving windows. (C) Total historical annual rainfall rates retrieved from flood layers using the four methods. Some intervals saw rates five times the average annual modern (2000 to 2021) rainfall of 31 mm/year. Plotted in orange is the annual TSI curve of Lean (22) smoothed with a 100-year moving window. Four episodes of low TSI and high rainfall are apparent (i through iv, highlighted in gray). Lomb-Scargle power spectra of the historical annual rainfall derived using methods 1 and 2 (D). Both return significant (99% confidence interval) periodicities centered at ~180 and ~500 years. The same periodicities are returned by methods 3 and 4 (omitted for brevity). (E) shows a continuous-wavelet transform (CWT) for detrended time series of annual rainfall (method 1) and TSI for the period where the two records overlap (850 to 1810 CE). In the CWT panels, red areas represent positive amplitude and blue areas indicate negative amplitude. In the semblance panel, a negative correlation between rainfall and TSI is sustained throughout the record (depicted as dark blue).

different age calibrations. Over this time span, age discrepancies between the two histories might approach 100 years.

A spectral analysis of the TSI record returned significant periodicities at 512, 356, 212, 125, 100, and 83 years. Similar analysis of methods 1 and 2 rainfall records found peaks centered at 500 and 180 years (Fig. 5D). The 180-year rainfall one may be linked to the Suess/de Vries cycle of 190- to 230-year solar excursions (23, 24). In addition, the 500-year cycle may be attributed to a ~520-year unnamed cycle from Bond *et al.* (25, 26). Following Cooper and Cowan (27), we next applied semblance analyses using continuous-wavelet transforms on detrended TSI and rainfall records. Semblance analysis (Fig. 5E) reveals a prominent inverse correlation between rainfall and TSI over time.

Physics-based simulation of flood layer deposition into the brine pool

Figure 5C plots estimated historical annual rainfall rates at the NEOM site based on the core flood layers and empirical formulas for rainfall and layer thickness. That might be the end of the story, but we think there is value in exploring physics-based models of sediment transport through the watershed, out to sea, and lastly onto the seafloor. We use the “Tsunami Squares” approach to do this (Supplementary Materials) and simulate 40 mm of rain above 30 mm soak-in amount falling into the brine pool’s watershed in 1 hour.

Figure 6 and supplementary movie S1 show the response of the entire 330-km² catchment area to this rain event. The brown shades offshore track sediment that has already settled to the seabed. This material

would be invisible from orbit. The thin white contours track sediment suspended in the water column. This cloud might be visible from orbit and comparable to the one imaged in Figure 1. Figure 6A shows the situation at $T = 1$ hour, just as the 13.2 million m³ of rain stopped falling. Onshore at that time, 6.9 million m³ of water carrying 0.24 million m³ of suspended sediment flowed down at an average speed of 2.46 m/s. Sediment concentration totaled $0.24/(6.9 + 0.24) = 3.38\%$. This aligns with the 3% concentration that Alexandrov *et al.* (28) reported flowing out of an ephemeral channel in the Negev Desert (Israel) after a comparable rain event. Offshore, 0.14 million m³ of sediment suspended in the plume expanded at an average speed of 0.86 m/s. In addition, 0.01 million m³ had already deposited on the seabed covering 6 km². After 11 ½ hours, the simulation deposits a flood layer 7.4 mm thick at the pool. Noteworthy is that empirical Eq. 21 (Materials and Methods) predicts a compatible layer thickness of $(70 - 30)/5 = 8$ mm for this amount of rain.

Overall, the physics-based TS simulation supports the empirical rainfall estimates from the cores, while providing a quantitative and visual presentation of the surface-plume origin of the brine pool’s flood layers as we imagine it.

DISCUSSION

Wet Arabia in the Late Holocene

The most obvious lesson from the NEOM brine pool is that the modern instrument record represents a dry extreme, as also emphasized by

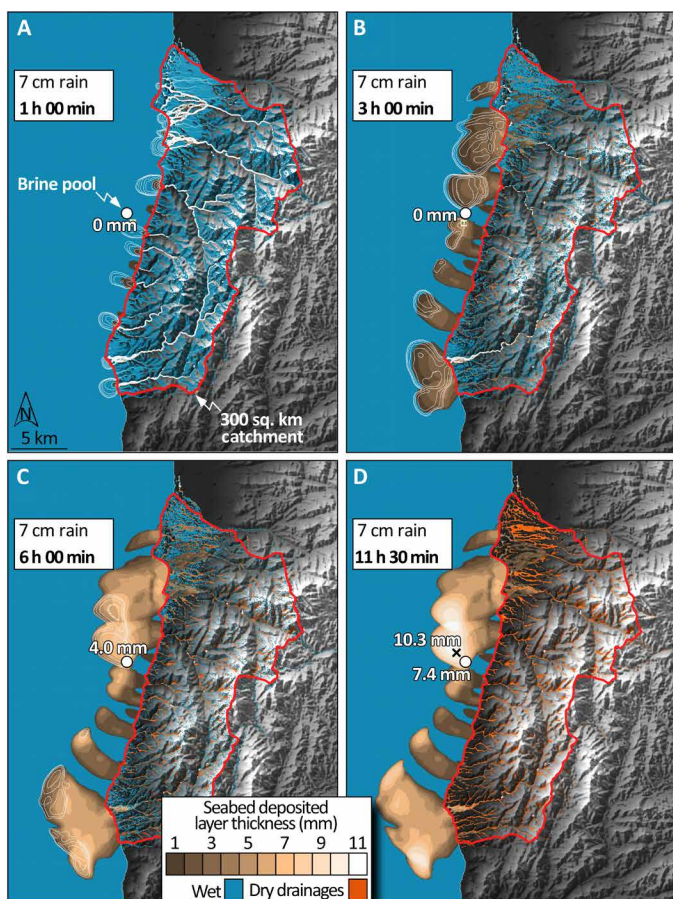


Fig. 6. Full basin TS simulation of 4 cm of rain over 3 cm of soak-in. Status of the sediment plume tracked after 1 hour (A), 3 hours (B), 6 hours (C), and 11 ½ hours (D). White contours represent the suspended sediment concentrations offshore. With time, the plumes discharged from the wadi mouths expand in area and sink. The thickness of the deposited mud drape is tracked by brown shading. The flash-floods deposit a 7.4-mm flood layer into the brine pool and as much as 10.3 mm a short distance away. Animation as supplementary movie S1.

Cook *et al.* (29) in the Mediterranean and by Flohr *et al.* (30) in Iraq. Our entire deep-sea record saw rainfalls greater than twice that of today. Early eyewitnesses support a wet antiquity.

In 167 BC, Agatharchides of Cnidus traveled down the Red Sea Saudi coast. In what is now the NEOM region, Agatharchides reports “abundant lion, leopard, wolves, and lotus as tall as a man” (31). The abundance of carnivores mentioned in this account indicates how extensive vegetation must have been—lions require large herbivores to feed on. The vast majority of lions in Africa today inhabit savannahs with an annual rainfall of 300 to 1500 mm.

Our cores pick up the story after 500 CE where four periods were particularly soured (gray bars, Fig. 5): the onset and end of the Medieval Warm Period and the onset and mid-point of the Little Ice Age. Of these, the onset of the Little Ice Age is the wettest by far. Between 1400 and 1550 CE, flashflood layers were 5 times more frequent than present, annual rainfall was 4 to 5 times greater, and the rate of terrigenous mud accumulation was 10 times higher. For the other three periods identified in Fig. 5, the climate was three to four times rainier than present.

Ottoman texts tell that by the late 1590s, Anatolia and Syria suffered a succession of cold, snowy winters that led to the death of hundreds of thousands (perhaps millions) of villagers (32). The Ottoman Empire fell into crisis because of a mix of famine, flight, and disease driven by widespread violence related to unpredictable climate (33, 34). The Celali Rebellion (1590 to 1610 CE, Fig. 5), the most persistent internal challenge to state power in the Empire’s existence, caps this crisis. The chronicler I. Peçevi reports that the Bosphorus completely froze over in February 1621, temporarily connecting European and Asian shores (34). Our cores suggest that rainfall into the pool’s catchment was more than triple the 31 mm/year of the modern era at that time. Only 100 years earlier, rains were five times fiercer than present.

Felis *et al.* (35) report the period 1750 to 1850 CE to be dry, based on isotopes from one coral sampled offshore the Sinai, 100 km south of the brine pool. Our cores concur that peak wetness had passed by 1750 CE, but still indicate the period to be rainier than present, by a factor of 2 at least. Eyewitnesses confirm our study area was wet at that time. In 1826, Ruppel approached Al Bad’, a town in the NEOM region 40 km inland from the brine pool. He wrote on July 11, “for although for several months no rain fell in the area, a mass of water, whose reflection in some places is a foot deep in many places and was fifty strides wide.” He continued, “the banks were with thick bushes overgrown, and along the banks there were numerous date palms.” Also consider A. Abdillah Ibn Ayas [1516, quoted by Burton, 1878 (36)] who records “springs of running water” and the wetlands reed *Arundo donax* growing in Aynunah (in NEOM). Burton also found springs, a large pool and same species of reed there in 1877, but all have now disappeared. Burton traveled down the route of the modern coast road. Before reaching Wadi Sharma, Burton was blocked by terrain “too marshy for their camels.” This area is a dry, dusty desert today. In the same account, Burton mentions the island of Umm Maksur and states it to be wooded. Today, not a single tree lives there.

Controls on Late Holocene hydroclimate in Arabia

We hypothesize that the regional rainfall changes revealed in our proxy record represent a radiatively driven shift in atmospheric circulation. There is abundant evidence that low TSI was an important forcing for the Little Ice Age in the Northern Hemisphere (22, 37–40). Moreover, Little Ice Age studies suggest that weak TSI increased rainfall at least as far south as southern Italy and North Africa. Our deep-sea record confirms that northern Arabia experienced the same Little Ice Age wet shift as reported in those other places.

Speleothems (41) and tree rings (42, 43) from the Moroccan Atlas Mountains indicate a wet Little Ice Age there. These studies implicate a negative phase of the North Atlantic Oscillation (NAO) as a rainfall driver, with a southward shifted jet stream delivering above-normal rain to southern Europe and Arabia (44–47). Alternatively, Hu *et al.* (48) ascribe the wet Little Ice Age shift in Italy to anomalously high atmospheric pressure over Northern Europe—so called “atmospheric ridging.” This phenomenon, the authors argue, splits the jet stream away from Central and Northern Europe and brings rainfall farther south. Regardless of the mechanism, our cores implicate changes in jet stream tracks that transport rainfall southward during cold periods of the Late Holocene.

Semblance analyses of TSI and rainfall histories show them to be inversely correlated (Fig. 5E). Evidently, a tiny decrease in annual TSI of 0.7 W m^{-2} (0.05%) increased annual rainfall fivefold in the

Gulf of Aqaba (Fig. 5B). On the basis of the models of Ammann *et al.* (49), a 0.7-W m⁻² irradiance drop translates to a global cooling of less than 0.07°C. Apparently for arid northern Arabia, processes like atmospheric ridging or NAO amplify this tiny decrease in temperature to a disproportionally large increase in rain. As the region rapidly urbanizes, our documentation of the wide variability of Late Holocene rains should be considered in flashflood preparedness and future hydroclimate trajectories.

MATERIALS AND METHODS

Retrieving historical rainfall rates from core layer statistics

Power law statistics

It is reasonable to imagine that time intervals with more and thicker core layers generally correspond to time intervals with more frequent and intense rains. To quantify this notion, we propose that both rainfall and layer statistics follow power laws like

$$N_{R>}(R) = N_{R>}(R_{\min}) 10^{-b_r(R-R_{\min})} \tag{1}$$

$$N_{T>}(T) = N_{T>}(T_{\min}) 10^{-b_t(T-T_{\min})} \tag{2}$$

$N_{R>}(R)$ and $N_{T>}(T)$ are the annual fall rate of rain amounts greater than R , and the annual production rate of layers of thickness greater than T , respectively. They both have units of number/year. R_{\min} and T_{\min} represent minimum values. To emphasize their “straight line” form for regression analysis, sometimes Eqs. 1 and 2 are written as

$$\log[N_{R>}(R)] = a_r(R_{\min}) - b_r(R - R_{\min}) \tag{3}$$

$$\log[N_{T>}(T)] = a_t(T_{\min}) - b_t(T - T_{\min}) \tag{4}$$

with

$$a_r(R_{\min}) = \log[N_{R>}(R_{\min})] \tag{5}$$

$$a_t(T_{\min}) = \log[N_{T>}(T_{\min})] \tag{6}$$

The positive coefficient pairs (a_r, a_t) and (b_r, b_t) are called “ a values” and “ b values.” Equations 1 and 2 can be integrated to form total annual rainfall and total annual layer thickness

$$R_{T>}(R_{\min}) = \int_{R_{\min}}^{\infty} \left[\frac{dN_{R>}(R)}{dR} \right] R dR \tag{7}$$

$$T_{T>}(T_{\min}) = \int_{T_{\min}}^{\infty} \left[\frac{dN_{T>}(T)}{dT} \right] T dT \tag{8}$$

Given

$$\frac{dN_{R>}(R)}{dR} = -b_r \ln(10) N_{R>}(R) \tag{9}$$

$$\frac{dN_{T>}(T)}{dT} = -b_t \ln(10) N_{T>}(T) \tag{10}$$

Equations 7 and 8 become

$$\begin{aligned} R_{T>}(R_{\min}) &= N_{R>}(R_{\min}) \left[R_{\min} + \frac{1}{b_r \ln(10)} \right] \\ &= 10^{a_r(R_{\min})} \left[R_{\min} + \frac{1}{b_r \ln(10)} \right] \end{aligned} \tag{11}$$

$$\begin{aligned} T_{T>}(T_{\min}) &= N_{T>}(T_{\min}) \left[T_{\min} + \frac{1}{b_t \ln(10)} \right] \\ &= 10^{a_t(T_{\min})} \left[T_{\min} + \frac{1}{b_t \ln(10)} \right] \end{aligned} \tag{12}$$

Equations 11 and 12 have units of millimeters per year.

Actual rainfall totals versus core rainfall totals—Wadi activation threshold and “invisible rain”

A goal of this work is to extract total historical rainfall rates from core flood-layer statistics. As such, the various “ a ,” “ b ,” “ $N_{>}$,” “ $R_{T>}$,” and “ $T_{T>}$ ” values will be functions of time epoch t_e , such as $a_r(T_{\min}, t_e)$, $b_t(t_e)$, $N_{T>}(T_{\min}, t_e)$, $R_{T>}(T_{\min}, t_e)$, etc. A hurdle, however, blocks our path, the Wadi Activation Threshold, R_{ACT} , the rain amount needed to induce a flood that runs to the sea and deposits a layer of T_{\min} in the brine pool. We have already concluded that $R_{ACT} = 35$ mm for $T_{\min} = 1$ mm, the thinnest unmistakable layer. Any rainstorm less than this does not show up in the cores. On an annual basis, how much might this invisible rain amount to? Using Eq. 11, the ratio of annual rainfall from storms greater than $R_{T>}(R_{ACT})$ to the total annual rainfall $R_{T>}(0)$ is

$$\frac{R_{T>}(R_{ACT})}{R_T^{corr} R_{T>}(0)} = 10^{-b_r R_{ACT}} [1 + b_r \ln(10) R_{ACT}] \tag{13}$$

If $b_r = 0.05/\text{mm}$, $R_T^{corr} = 1.44$ (see Eq. 24), and $R_{ACT} = 35$ mm, then Eq. 13 equals 0.062. Thus, nearly 94% of the annual rainfall comes from storms less than 35 mm that leave no trace in the cores. How to account for invisible rain? This takes a bit of scaling magic.

Suppose that we knew $N_{R>}(R_{ACT}, t_e)$, the annual numbers of rainfalls greater than R_{ACT} at epoch t_e . Then, the total annual rainfall above R_{\min} would be

$$R_{T>}(R_{\min}, t_e) = N_{R>}(R_{ACT}, t_e) 10^{b_r(R_{ACT}-R_{\min})} \left[R_{\min} + \frac{1}{b_r \ln(10)} \right] \tag{14}$$

Alternatively, suppose that we knew $R_{T>}(R_{ACT}, t_e)$, the total annual rainfall of rains greater than R_{ACT} at epoch t_e . Then, the total annual rainfall rain greater than R_{\min} would then be

$$R_{T>}(R_{\min}, t_e) = R_{T>}(R_{ACT}, t_e) 10^{b_r(R_{ACT}-R_{\min})} \frac{\left[R_{\min} + \frac{1}{b_r \ln(10)} \right]}{\left[R_{ACT} + \frac{1}{b_r \ln(10)} \right]} \tag{15}$$

If $b_r = 0.05/\text{mm}$, $R_{ACT} = 35$ mm, and $R_{\min} = 0$, then Eqs. 14 and 15 reduce to simple scalings of the number of core rains or the total core rainfall corrected by R_T^{corr} (24)

$$R_{T>}(0, t_e) = N_{R>}(35 \text{ mm}, t_e)[488.4 \text{ mm}] R_T^{corr}$$

$$= N_{R>}(35 \text{ mm}, t_e)[703.3 \text{ mm}] \quad (16)$$

$$R_{T>}(0, t_e) = R_{T>}(35 \text{ mm}, t_e)[11.2] R_T^{corr}$$

$$= R_{T>}(35 \text{ mm}, t_e)[16.13] \quad (17)$$

The inverse of 16.13 is 0.062, so Eq. 17 is just a restatement of Eq. 13, that core rainfall totals equal just a small fraction of the actual rainfall totals.

Methods 1 and 2: Estimate $N_{R>}(R_{ACT}, t_e)$

These methods assume that the annual production rate of layers greater than $T_{min} = 1 \text{ mm}$ at epoch t_e corresponds to the annual fall rate of rains greater than $R_{ACT} = 35 \text{ mm}$ at that epoch, that is

$$N_{R>}(35 \text{ mm}, t_e) = N_{T>}(1 \text{ mm}, t_e) \quad (18)$$

Method 1 simply counts layers and divides by the epoch duration

$$N_{T>}(1 \text{ mm}, t_e) = \frac{1}{\Delta T} \sum_N C(T_N) \quad (19)$$

The sum covers all layers of thickness T_N in epoch t_e and $C(T_N)$ equals 1 if layer thickness T_N exceeds 1 mm and is zero otherwise.

Rather than simply counting layers greater than 1 mm, method 2 does a least-squares fit (Eq. 4) of all layer thicknesses greater than 1 mm in the epoch and estimates the annual production rate by

$$N_{T>}(1 \text{ mm}, t_e) = 10^{a_r(1 \text{ mm}, t_e)} \quad (20)$$

Because the least-squares fit tries to account for the distribution of layer thickness, not just the total number of layers as in Eq. 19, Eq. 20 may be a better estimate. In any given epoch, however, the number of layers can be few and the fit can be uncertain.

Methods 3 and 4: Estimate $R_{T>}(R_{ACT}, t_e)$

These methods assume that a core layer of thickness $T > 1 \text{ mm}$ requires a rainfall $R(T)$ of

$$R(T) = 30 \text{ mm} + 5 T \quad (21)$$

We have already established that 30 mm (R_{Soak}) of rain is needed to reach the sea, and that 5 mm extra is needed to make a flood layer of 1 mm at the brine pool (Supplementary Materials). The black triangles in Fig. 4A scale core layer thickness to rainfall. The fact that these scaled values nicely track the power-law fit independently determined from the IMERG data supports Eq. 21.

Method 3 simply counts core layers scaled by Eq. 21 and divides by the epoch duration

$$R_{T>}(35 \text{ mm}, t_e) = \frac{1}{\Delta T} \sum_N C(T_N) R(T_N) \quad (22)$$

Again, the sum covers all layers of thickness T_N in the epoch t_e and $C(T_N)$ equals 1 if layer thickness T_N exceeds 1 mm and is zero otherwise.

Rather than simply counting scaled layers, method 4 does a least-squares fit (Eq. 4) of all layer thicknesses greater than 1 mm in the epoch and estimates the annual production rate

$$R_{>}(35 \text{ mm}, t_e) = 10^{a_r(1 \text{ mm}, t_e)} \left[30 \text{ mm} + \frac{5}{b_r(t_e) \ln(10)} \right] \quad (23)$$

Bottom line

Equations 18, 19, 20, 22, and 23 when scaled by Eq. 16 or 17 represent reasonably independent values of total historical annual rainfall as determined from our cores, including the contribution from invisible rains.

The low rain tail correction

The frequency of IMERG rain events greater than 3 mm is well fit by a single power law distribution with a slope of $b_r = 0.05/\text{mm}$ (blue line, Fig. 4A). It is seen, however, that the rates of IMERG rains less than 3 mm steepen sharply (slope $b_r^{tail} = 0.22/\text{mm}$). These rains are severely undercounted by the power-law fit to the IMERG data. At first glance, the “low rain tail” might represent rains that failed to reach the ground. However, the surface-sited Eilat gauge records the same tail, so it is likely real. In addition, we already counted the low rain tail in our analysis of IMERG satellite data when establishing the modern rainfall rate of 31.33 mm/year (Fig. 3). Therefore, a correction factor R_T^{corr} needs to be introduced to all single “power law” rainfall values including those used by Eqs. 13 through 17 that neglect the tail. The correction factor is

$$R_T^{corr} = 10^{-b_r 3 \text{ mm}} \left(1 + \frac{b_r 10^{b_r^{tail} 3 \text{ mm}}}{b_r^{tail}} \right) = 1.44 \quad (24)$$

R_T^{corr} should multiply any single power law–derived value for annual rainfall to account for the low rain tail. It is a bit unusual that rains $< 3 \text{ mm}$ contribute so significantly (44%) to the total, but their numbers outweigh their size.

Variations in annual rainfall estimates versus watershed state

This paper considered the “state” of the watershed to be constant over 1.6 thousand years. By state, we mean the ability of a rainfall of $T \text{ mm}$ to mobilize sediment. In reality, the state of the watershed could vary over both long and short timescales.

Long-term evolution of watershed state might involve anthropogenic activities like herding. Apart from the thin coastal strip, however, the mountains are so high and rugged as to render the land inaccessible. Even in modern times, herding is exceedingly low, if present at all. In antiquity, before the introduction of firearms and motorized vehicles, predation from abundant lions, leopards, and wolves would have precluded herding entirely. Short-term variations in watershed state might involve rainfall amounts, or time intervals between storms. For instance, the surface of the watershed might be “drought-hardened” during times of infrequent rain (50). A “watershed-softened” scenario is also possible, for instance when sediment accumulates in wadis and elsewhere at times of moderate rainfall, before being remobilized by a major flashflood.

In our approach, watershed state is entirely encapsulated in the two numbers in Eq. 21

$$R(T) = 30 \text{ mm} + 5 T \quad (\text{Nominal State } S_0)$$

$R(T)$ is the amount of rain required to form a layer of thickness $T \text{ mm}$ at the brine pool. The first number, R_{Soak} , defines the quantity of rain for first runoff to reach the sea (determined from SAR sensing to be 30 mm—Supplementary Materials). The second number, R_{Extra} ,

relates to the concentration of sediment within that runoff (eq. S26—Supplementary Materials). A smaller R_{Extra} means a higher sediment concentration, that is, a softer or more erodible watershed. A larger R_{Extra} means a lower concentration of sediment, that is, a harder or less erodible watershed.

To investigate the influence of watershed state on our rainfall retrievals, we propose two end members

$$R(T) = 27 \text{ mm} + 10 T \quad \text{Hard Watershed} \quad (\text{State S1})$$

$$R(T) = 33 \text{ mm} + 2.5 T \quad \text{Soft Watershed} \quad (\text{State S2})$$

In a hard watershed (S1), 10% less rain is needed to generate first runoff, but that runoff has one-half the concentration of sediment versus (S0). In a soft watershed (S2), 10% more rain is needed to generate first runoff, but that runoff has twice the concentration of sediment versus (S0). For methods 1 and 2, Eq. 14 expresses the total annual rainfall given the state parameter $R_{\text{ACT}} = R(T_{\text{min}} = 1 \text{ mm})$ and the number of layers $T > 1 \text{ mm}$. Layer counts come from cores and are independent of watershed state, so only R_{ACT} differences of 35, 37 and 35.5 mm matter in Eq. 14, thus

$$R_{T>} (R_{\text{min}}, \text{S1}) = 10^{0.05(37-35)} R_{T>} (R_{\text{min}}, \text{S0}) = 1.25 R_{T>} (R_{\text{min}}, \text{S0})$$

and

$$R_{T>} (R_{\text{min}}, \text{S2}) = 10^{0.05(35.5-35)} R_{T>} (R_{\text{min}}, \text{S0}) = 1.06 R_{T>} (R_{\text{min}}, \text{S0})$$

For the hard and soft watershed states (S1 and S2), our annual rainfall estimates should be increased by 25 and 6%, respectively, versus nominal values (S0). Results for methods 3 and 4 using Eq. 15 are similar.

According to eq. S26 (Supplementary Materials), sediment concentrations for the S1 and S2 scenarios would be 1.4 to 3.5% and 5.4 to 13.8%, respectively. One could propose other states, but we consider these drought-hardened and watershed-softened cases extreme. Last, keep in mind that each of our 100-year windows sample several storms, so short-term changes in state would tend to average out in our annual rainfall estimates.

Supplementary Materials

The PDF file includes:

Supplementary Text

Figs. S1 to S5

Table S1

Legends for movies S1 and S2

References

Other Supplementary Material for this manuscript includes the following:

Movies S1 and S2

REFERENCES AND NOTES

- H. W. Arz, F. Lamy, J. Pätzold, P. J. Müller, M. Prins, Mediterranean moisture source for an Early-Holocene humid period in the Northern Red Sea. *Science* **300**, 118–121 (2003).
- A. G. Parker, A. S. Goudie, S. Stokes, K. White, M. J. Hodson, M. Manning, D. Kennet, A record of Holocene climate change from lake geochemical analyses in southeastern Arabia. *Quatern. Res.* **66**, 465–476 (2006).
- S. J. Purkis, G. P. Rowlands, B. M. Riegl, P. G. Renaud, The paradox of tropical karst morphology in the coral reefs of the arid Middle East. *Geology* **38**, 227–230 (2010).
- F. Gasse, Hydrological changes in the African tropics since the Last Glacial Maximum. *Quat. Sci. Rev.* **19**, 189–211 (2000).
- P. Hoelzmann, H.-J. Kruse, F. Rottinger, Precipitation estimates for the eastern Saharan palaeomonsoon based on a water balance model of the West Nubian Palaeolake Basin. *Glob Planet Change* **26**, 105–120 (2000).
- J. Lelieveld, Y. Proestos, P. Hadjinicolaou, M. Tanarhte, E. Tyrllis, G. Zittis, Strongly increasing heat extremes in the Middle East and North Africa (MENA) in the 21st century. *Clim. Change* **137**, 245–260 (2016).
- W. Cramer, J. Guiot, M. Fader, J. Garrabou, J.-P. Gattuso, A. Iglesias, M. A. Lange, P. Lionello, M. C. Llasat, S. Paz, J. Peñuelas, M. Snoussi, A. Toreti, M. N. Tsimplis, E. Xoplaki, Climate change and interconnected risks to sustainable development in the Mediterranean. *Nat. Clim. Chang.* **8**, 972–980 (2018).
- G. Zittis, P. Hadjinicolaou, M. Fnaies, J. Lelieveld, Projected changes in heat wave characteristics in the eastern Mediterranean and the Middle East. *Reg. Environ. Change* **16**, 1863–1876 (2016).
- G. Zittis, Observed rainfall trends and precipitation uncertainty in the vicinity of the Mediterranean, Middle East and North Africa. *Theor. Appl. Climatol.* **134**, 1207–1230 (2018).
- P. O. Hopcroft, P. J. Valdes, Paleoclimate-conditioning reveals a North Africa land-atmosphere tipping point. *Proc. Natl. Acad. Sci. U.S.A.* **118**, e2108783118 (2021).
- U. Dayan, R. Abramski, Heavy rain in the Middle East related to unusual jet stream properties. *Bull. Am. Meteorol. Soc.* **64**, 1138–1140 (1983).
- Z. Ben-Avraham, G. Almagor, Z. Garfunkel, Sediments and structure of the Gulf of Elat (Aqaba)—Northern Red Sea. *Sediment. Geol.* **23**, 239–267 (1979).
- H. Fricke, Deep-water exploration of the Red Sea by submersible, in *Deep Sea and Extreme Shallow-Water Habitats: Affinities and Adaptations*, F. Uiblein, J. Ott, M. Stachowitsch, Eds. (Österreichische Akad. der Wiss, 1996), pp. 67–89.
- K. M. Straub, R. A. Duller, B. Z. Foreman, E. A. Hajek, Buffered, incomplete, and shredded: The challenges of reading an imperfect stratigraphic record. *Case Rep. Med.* **125**, e2019JF005079 (2020).
- Z. Steiner, B. Lazar, S. Levi, S. Tsroya, O. Pelled, R. Bookman, J. Erez, The effect of bioturbation in pelagic sediments: Lessons from radioactive tracers and planktonic foraminifera in the Gulf of Aqaba, Red Sea. *Geochim. Cosmochim. Acta* **194**, 139–152 (2016).
- T. Katz, H. Ginat, G. Eyal, Z. Steiner, Y. Braun, S. Shalev, B. N. Goodman-Tchernov, Desert flash floods form hyperpycnal flows in the coral-rich Gulf of Aqaba, Red Sea. *Earth Planet. Sci. Lett.* **417**, 87–98 (2015).
- O. M. Bialik, R. Bookman, H. Elyashiv, A. Marietou, R. Saar, T. Rivlin, N. Taha, T. Benaltabet, N. Lotem, E. Funaro, G. Antler, Tropical storm-induced disturbance of deep-water porewater profiles, Gulf of Aqaba. *Mar. Geol.* **453**, 106926 (2022).
- S. J. Purkis, H. Shernisky, P. K. Swart, A. Sharifi, A. Oehlert, F. Marchese, F. Benzioni, G. Chimenti, G. Duchâtellier, J. Klaus, G. P. Eberli, L. Peterson, A. Craig, M. Rodrigue, J. Titschack, G. Kolodziej, A. Abdulla, Discovery of the deep-sea NEOM Brine Pools in the Gulf of Aqaba, Red Sea. *Commun. Earth Environ.* **3**, 146 (2022).
- G. Huffman, D. Bolvin, D. Braithwaite, K. Hsu, R. Joyce, P. Xie, Integrated multi-satellite retrievals for GPM (IMERG), version 4.4 (NASA's Precipitation Processing Center, 2014).
- E. Frucht, A. Salamon, E. Gal, H. Ginat, M. Grigorovitch, R. Shem Tov, S. Ward, A fresh view of the tsunami generated by the Dead Sea Transform, 1995 M_w 7.2 Nuweiba Earthquake, along the Gulf of Elat–Aqaba. *Seismol. Res. Lett.* **90**, 1483–1493 (2019).
- H. Vasyura-Bathke, A. Steinberg, F. Krüger, G. Feng, P. M. Mai, S. Jónsson, Discontinuous transensional rupture during the Mw 7.2 1995 Gulf of Aqaba earthquake. *Seismica* **3**, 10.26443/seismica.v3i1.1135 (2024).
- J. L. Lean, Estimating solar irradiance since 850 CE. *Earth Space Sci.* **5**, 133–149 (2018).
- F. Steinhilber, J. A. Abreu, J. Beer, I. Brunner, M. Christl, H. Fischer, U. Heikkilä, P. W. Kubik, M. Mann, K. G. McCracken, 9,400 years of cosmic radiation and solar activity from ice cores and tree rings. *Proc. Natl. Acad. Sci. U.S.A.* **109**, 5967–5971 (2012).
- L. Ma, J. M. Vaquero, New evidence of the Suess/de Vries cycle existing in historical naked-eye observations of sunspots. *Open Astronomy* **29**, 28–31 (2020).
- G. Bond, W. Showers, M. Cheseby, R. Lotti, P. Almasi, P. deMenocal, P. Priore, H. Cullen, I. Hajdas, G. Bonani, A pervasive millennial-scale cycle in North Atlantic Holocene and glacial climates. *Science* **278**, 1257–1266 (1997).
- G. Bond, B. Kromer, J. Beer, R. Muscheler, M. N. Evans, W. Showers, S. Hoffmann, R. Lotti-Bond, I. Hajdas, G. Bonani, Persistent solar influence on North Atlantic climate during the Holocene. *Science* **294**, 2130–2136 (2001).
- G. R. J. Cooper, D. R. Cowan, Comparing time series using wavelet-based semblance analysis. *Comput. Geosci.* **34**, 95–102 (2008).
- Y. Alexandrov, J. B. Laronne, I. Reid, Suspended sediment concentration and its variation with water discharge in a dryland ephemeral channel, northern Negev, Israel. *J. Arid Environ.* **53**, 73–84 (2003).
- B. I. Cook, K. J. Anchukaitis, R. Touchan, D. M. Meko, E. R. Cook, Spatiotemporal drought variability in the Mediterranean over the last 900 years. *J. Geophys. Res.—Atmos.* **121**, 2060–2074 (2016).
- P. Flohr, D. Fleitmann, E. Zorita, A. Sadekov, H. Cheng, M. Bosomworth, L. Edwards, W. Matthews, R. Matthews, Late Holocene droughts in the Fertile Crescent recorded in a speleothem from northern Iraq. *Geophys. Res. Lett.* **44**, 1528–1536 (2017).
- S. M. Burstein, H. Society, *On the Erythraean Sea* (Hakluyt Society London, 1989).
- S. White, A model disaster: From the Great Ottoman Panzootic to the cattle plagues of early modern Europe, in *Plague and Contagion in the Islamic Mediterranean*, N. Varlik, Ed. (Amsterdam University Press, 2017), pp. 91–116.
- D. Kaniewski, E. Van Campo, E. Paulissen, H. Weiss, J. Bakker, I. Rossignol, K. Van Lerberghe, The medieval climate anomaly and the little Ice Age in coastal Syria inferred from pollen-derived palaeoclimatic patterns. *Glob Planet Change* **78**, 178–187 (2011).
- S. White, *Water on Sand: Environmental Histories of the Middle East and North Africa* (Oxford University Press, 2012).

35. T. Felis, M. Ionita, N. Rimbu, G. Lohmann, M. Kölling, Mild and arid climate in the Eastern Sahara-Arabian Desert during the Late Little Ice Age. *Geophys. Res. Lett.* **45**, 7112–7119 (2018).
36. R. F. Burton, *The Gold-Mines of Midian and the Ruined Midianite cities: A Fortnight's Tour in North-Western Arabia* (C. Kegan Paul & Company, 1878).
37. M. Free, A. Robock, Global warming in the context of the Little Ice Age. *J. Geophys. Res.* **104**, 19057–19070 (1999).
38. D. T. Shindell, G. A. Schmidt, M. E. Mann, D. Rind, A. Waple, Solar forcing of regional climate change during the Maunder Minimum. *Science* **294**, 2149–2152 (2001).
39. G. H. Miller, Á. Geirsdóttir, Y. Zhong, D. J. Larsen, B. L. Otto-Bliesner, M. M. Holland, D. A. Bailey, K. A. Refsnider, S. J. Lehman, J. R. Southon, C. C. Anderson, H. Björnsson, T. Thordarson, Abrupt onset of the Little Ice Age triggered by volcanism and sustained by sea-ice/ocean feedbacks. *Geophys. Res. Lett.* **39**, L02708 (2012).
40. S. Brönnimann, J. Franke, S. U. Nussbaumer, H. J. Zumbühl, D. Steiner, M. Trachsel, G. C. Hegerl, A. Schurer, M. Worni, A. Malik, J. Flückiger, C. C. Raible, Last phase of the Little Ice Age forced by volcanic eruptions. *Nat. Geosci.* **12**, 650–656 (2019).
41. Y. Ait Brahimi, H. Cheng, A. Sifeddine, J. A. Wassenburg, F. W. Cruz, M. Khodri, L. Sha, N. Pérez-Zanón, E. H. Beraouz, J. Apaéstegui, J.-L. Guyot, K. P. Jochum, L. Bouchaou, Speleothem records decadal to multidecadal hydroclimate variations in southwestern Morocco during the last millennium. *Earth Planet. Sci. Lett.* **476**, 1–10 (2017).
42. J. Esper, D. Frank, U. Büntgen, A. Verstege, J. Luterbacher, E. Xoplaki, Long-term drought severity variations in Morocco. *Geophys. Res. Lett.* **34**, L17702 (2007).
43. J. A. Wassenburg, A. Immenhauser, D. K. Richter, A. Niedermayr, S. Riechelmann, J. Fietzke, D. Scholz, K. P. Jochum, J. Fohlmeister, A. Schröder-Ritzrau, A. Sabaoui, D. F. C. Riechelmann, L. Schneider, J. Esper, Moroccan speleothem and tree ring records suggest a variable positive state of the North Atlantic Oscillation during the Medieval Warm Period. *Earth Planet. Sci. Lett.* **375**, 291–302 (2013).
44. R. Schiemann, D. Lüthi, C. Schär, Seasonality and interannual variability of the Westerly Jet in the Tibetan Plateau region. *J. Climate* **22**, 2940–2957 (2009).
45. A. Sharifi, L. N. Murphy, A. Pourmand, A. C. Clement, E. A. Canuel, A. Naderi Beni, H. A. K. Lahijani, D. Delanghe, H. Ahmady-Birgani, Early-Holocene greening of the Afro-Asian dust belt changed sources of mineral dust in West Asia. *Earth Planet. Sci. Lett.* **481**, 30–40 (2018).
46. Q. Ren, W. Wei, M. Lu, S. Yang, Dynamical analysis of the winter Middle East jet stream and comparison with the East Asian and North American jet streams. *J. Climate* **35**, 4455–4468 (2022).
47. W. Wei, Q. Ren, M. Lu, S. Yang, Zonal extension of the Middle East jet stream and its influence on the Asian Monsoon. *J. Climate* **35**, 4741–4751 (2022).
48. H.-M. Hu, C.-C. Shen, J. C. H. Chiang, V. Trouet, V. Michel, H.-C. Tsai, P. Valensi, C. Spötl, E. Starnini, M. Zunino, W.-Y. Chien, W.-H. Sung, Y.-T. Chien, P. Chang, R. Korty, Split westerlies over Europe in the early Little Ice Age. *Nat. Commun.* **13**, 4898 (2022).
49. C. M. Ammann, F. Joos, D. S. Schimel, B. L. Otto-Bliesner, R. A. Tomas, Solar influence on climate during the past millennium: Results from transient simulations with the NCAR Climate System Model. *Proc. Natl. Acad. Sci. U.S.A.* **104**, 3713–3718 (2007).
50. H. N. Le Houérou, Climate change, drought and desertification. *J. Arid Environ.* **34**, 133–185 (1996).
51. G. Duchâtellier, A. M. Oehlert, H. Shernisky, C. G. L. Pollier, P. K. Swart, B. Howes, S. J. Purkis, Sedimentary porewaters record regional tectonic and climate events that perturbed a deep-sea brine pool in the Gulf of Aqaba, Red Sea. *Sci. Total Environ.* **912**, 168804 (2024).
52. R. W. Reimer, P. J. Reimer, An online application for ΔR calculation. *Radiocarbon* **59**, 1623–1627 (2017).
53. C. Keller, Chron. j1: A Bayesian framework for integrated eruption age and age-depth modelling. *OSF (Open Science Framework)* **10**, 10.17605/osf.io/TQX3F (2018).
54. B. Schoene, M. P. Eddy, K. M. Samperton, C. B. Keller, G. Keller, T. Adatte, S. F. R. Khadri, U-Pb constraints on pulsed eruption of the Deccan Traps across the end-Cretaceous mass extinction. *Science* **363**, 862–866 (2019).
55. A. Govin, U. Holzwarth, D. Heslop, L. Ford Keeling, M. Zabel, S. Mulitza, J. A. Collins, C. M. Chiessi, Distribution of major elements in Atlantic surface sediments (36°N–49°S): Imprint of terrigenous input and continental weathering. *Geochem. Geophys. Geosyst.* **13**, Q01013 (2012).
56. L. Burone, L. Ortega, P. Franco-Fraguas, M. Mahiques, F. García-Rodríguez, N. Venturini, Y. Marin, E. Brugnoli, R. Nagai, P. Muniz, M. Bicego, R. Figueira, A. Salaroli, A multiproxy study between the Río de la Plata and the adjacent South-western Atlantic inner shelf to assess the sediment footprint of river vs. marine influence. *Cont. Shelf Res.* **55**, 141–154 (2013).
57. L. Perez, F. García-Rodríguez, T. J. J. Hanebuth, Variability in terrigenous sediment supply offshore of the Río de la Plata (Uruguay) recording the continental climatic history over the past 1200 years. *Clim. Past* **12**, 623–634 (2016).
58. S. J. Purkis, S. N. Ward, H. Shernisky, G. Chimienti, A. Sharifi, F. Marchese, F. Benzoni, M. Rodrigue, M. E. Raymo, A. Abdulla, Tsunamigenic potential of an incipient submarine landslide in the Tiran Straits. *Geophys. Res. Lett.* **49**, e2021GL097493 (2022).
59. B. Goodman Tchervov, T. Katz, Y. Shaked, N. Kupty, M. Kanari, T. Niemi, A. Agnon, Offshore evidence for an undocumented tsunami event in the 'low risk' Gulf of Aqaba-Eilat, Northern Red Sea. *PLOS ONE* **11**, e0145802 (2016).
60. Z. Bektaş, U. Avcı, M. Ribot, Y. Klinger, S. Jónsson, Seismo-turbidites reveal locations of major earthquakes during the past millennium in the Gulf of Aqaba, southern Dead Sea Fault. *Earth Planet. Sci. Lett.* **629**, 118595 (2024).
61. G. P. Rowlands, S. J. Purkis, B. M. Riegl, The 2005 coral-bleaching event Roatan (Honduras): Use of pseudoinvariant features (PIFs) in satellite assessments. *J. Spat. Sci.* **53**, 99–112 (2008).
62. M. Abrams, R. Crippen, H. Fujisada, ASTER Global Digital Elevation Model (GDEM) and ASTER Global Water Body Dataset (ASTWBD). *Remote Sens. (Basel)* **12**, 10.3390/rs12071156 (2020).
63. J. Wang, S. N. Ward, L. Xiao, Numerical modelling of rapid, flow-like landslides across 3-D terrains: A Tsunami Squares approach to El Picacho landslide, El Salvador, September 19, 1982. *Geophys. J. Int.* **201**, 1534–1544 (2015).
64. L. Xiao, S. N. Ward, J. Wang, Tsunami Squares approach to landslide-generated waves: Application to Gongjiafang Landslide, Three Gorges Reservoir, China. *Pure Appl. Geophys.* **172**, 3639–3654 (2015).
65. J. Wang, S. N. Ward, L. Xiao, Tsunami Squares modelling of the 2015 June 24 Hongyanzi landslide generated river tsunamis in Three Gorges Reservoir, China. *Geophys. J. Int.* **216**, 287–295 (2018).
66. S. J. Purkis, S. N. Ward, N. M. Fitzpatrick, J. B. Garvin, D. Slayback, S. J. Cronin, M. Palaseanu-Lovejoy, A. Dempsey, The 2022 Hunga-Tonga megatsunami: Near-field simulation of a once-in-a-century event. *Sci. Adv.* **9**, eadf5493 (2023).
67. F. Yao, I. Hoteit, L. J. Pratt, A. S. Bower, P. Zhai, A. Köhl, G. Gopalakrishnan, Seasonal overturning circulation in the Red Sea: 1. Model validation and summer circulation. *J. Geophys. Res.* **119**, 2238–2262 (2014).

Acknowledgments: We owe a debt of gratitude to our Saudi Arabian partners, NEOM, and to R. Bush, D. Colbourne, J. Munro, A. Khamis, and D. Rossel for supporting this study. We are similarly indebted to OceanX and the crew of OceanXplorer for their operational and logistical support. In particular, we would like to acknowledge A. Craig, O. Dieckhoff, E. Bason, L. Frühe, and K. von Krusenstiern for data acquisition, sample collection, and support of scientific operations aboard OceanXplorer. We would also like to thank OceanX Media for documenting and communicating this work with the public. Gratitude is extended to H. Graber and N. Thomas for advice with microwave sensing and to I. Enochs for CT scanning of cores. **Funding:** This work was supported by NEOM agreement no. SRA-ENV-2023-001/AWD-008854 (S.J.P.) and NSF Climate and Large-Scale Dynamics grant no. 2241752 (A.C.C.). **Author contributions:** S.J.P. designed the research. S.N.W. led the scaling of flood layers to rainfall and ran the physics-based transport models. M.I.C. and A.K. prepared and interpreted cores, while J.M.L. assembled the IMERG satellite rainfall record. A.C.C. provided climatology advice. A.S. and B.J.H. constructed age models, and F.B. and M.R. were instrumental in executing the research cruise. C.C. provided the perspective of rainfall in antiquity. S.J.P. and S.N.W. interpreted data and wrote the paper with input from all coauthors. **Competing interests:** The authors declare that they have no competing interests. **Data and materials availability:** All data needed to evaluate the conclusions in the paper are present in the paper and/or the Supplementary Materials.

Submitted 8 May 2024
Accepted 23 January 2025
Published 21 February 2025
10.1126/sciadv.adq3173